Deployment and Evaluation of a Low-Cost Sensor System for Atmospheric CO₂ Monitoring on a Sea-Air Interface Buoy

Jialu Liu[1,2], Pengfei Han[3*], Huiling Ouyang[1,4], Ning Zeng[5,6], Zhenfeng Wang[1], Jian Wang[1], Weiwei Fu[1,2], Honggang Lv[7], Wenhao Lin[8], Zheng Xia[1,9,10], Bo Yao[1,2, 11*]

[1]Department of Atmospheric and Oceanic Sciences and Institute of Atmospheric Sciences, Fudan University, Shanghai, 200438, China

[2]Shanghai Frontiers Science Center of Atmosphere-Ocean Interaction, Key Laboratory of Polar Atmosphere-Ocean-Ice System for Weather and Climate of Ministry of Education, and Shanghai Key Laboratory of Ocean-Land-Atmosphere Boundary Dynamics, Fudan University, Shanghai, 200438, China

[3]State Key Laboratory of Atmospheric Environment and Extreme Meteorology, Institute of Atmospheric Physics, Chinese Academy of Sciences, Beijing, 100029, China

[4]Observation and Research Station of Huaniaoshan East China Sea Ocean-Atmosphere Integrated Ecosystem, Ministry of Natural Resources, Shanghai, 200136, China

[5]Department of Atmospheric and Oceanic Science, University of Maryland, College Park, Maryland, 20742, USA

[6]Earth System Science Interdisciplinary Center, University of Maryland, College Park, Maryland, 20742, USA

[7]Key Laboratory of Marine Hazards Forecasting, National Marine Environmental Forecasting Center, Ministry of Natural Resources (MNR), Beijing, 100081, China; National Marine Environmental Forecasting Center, Beijing, 100081, China

[8]Zhejiang Environmental Monitoring Engineering, Co.Ltd., 310013, China

[9]Zhejiang Ecological and Environmental Monitoring Center, Hangzhou, 310012, China

[10]Zhejiang Key Laboratory of Ecological and Environmental Monitoring, Forewarning and Quality Control, Hangzhou, 310012, China

[11]National Observation and Research Station for Wetland Ecosystems of the Yangtze Estuary, Shanghai, 201112, China

Correspondence to: Bo Yao (yaobo@fudan.edu.cn); Pengfei Han (pfhan@mail.iap.ac.cn)

Abstract. Direct in-situ observation of marine CO_2 concentrations is, crucial for estimating air-sea CO_2 fluxes, yet such observations remain scarce. Drawn on experiences from urban CO_2 monitoring and buoy-based measurements, this study deployed a sea-air interface buoy platform in the northern South China Sea, near Maoming, Guangdong Province, China. This platform was equipped with three low-cost

5   SenseAir K30 sensors to enable continuous atmospheric CO_2 measurement. This paper presents the first detailed account of the methodology, encompassing hardware design, environmental corrections, land-based validation tests, offshore deployment procedures, and initial observational results. These findings thus provide valuable insights for advancing marine CO_2 observations practices. To mitigate the impacts of temperature, humidity, and pressure on sensor readings - while simultaneously compensating for zero-

10   drift - an environmental correction method was implemented. This approach significantly improved data accuracy: in land tests, the root mean square errors was reduced from 8.03 ppm to 3.64 ppm; in marine observations, the root mean square errors decreased from 24.26 ppm to 1.59 ppm. Importantly, this level of precision meets the requirements for resolving sea surface CO_2 dynamics (~420-480 ppm). Observed concentrations were consistent with HYSPLIT-simulated long-range atmospheric transport, revealing

15   the stable and homogeneous nature of the marine atmospheric boundary layer, with diurnal variations of approximately 3 ppm, and capturing localized or short-term fluctuations due to terrestrial carbon sources. These results demonstrate the effectiveness of the method, offering a low-cost, high-density solution for marine atmospheric CO_2 monitoring and providing key inputs for inversely estimating ocean carbon sink.

Keywords：marine atmospheric CO_2; low-cost sensors; environmental correction; buoy measurements

20 **1   Introduction**

Since the Industrial Revolution, less than half of the carbon emitted into the atmosphere by human activities remains in the atmosphere (Friedlingstein et al., 2020; Costa et al., 2023), highlighting the pivotal role of terrestrial and ocean sinks in regulating atmospheric CO_2 concentrations. From 2013 to 2022, the ocean absorbed and stored CO_2 approximately 26% of total anthropogenic CO_2 emissions

25 (Friedlingstein et al., 2023). The ocean stores a vast amount of CO_2, with inorganic carbon reservoir approximately 50 times greater than those in the atmosphere (Sabine et al., 2004). Therefore, studying oceanic CO_2 sources and sinks is crucial for developing mitigation strategies and mitigate climate change. The most widely and extensively applied, and long-established method for ocean carbon sink investigation involves measuring the partial pressure difference of CO_2 (ΔpCO_2) across the air-sea

30 interface (Song et al., 2023). Continuous observations used to calculate the air-sea CO_2 flux, providing the most direct characterization of the ocean carbon cycle system (Wanninkhof et al., 2019; Song et al., 2023).

Owing to the past several decades of continuous observations, a large amount of sea surface pCO_2 data has been accumulated, yet it remains insufficient relative to the vast ocean area. The Surface Ocean

35 CO_2 Atlas (SOCAT 2023) revealed that the ocean area covered by monthly CO_2 measurements has decreased by nearly half since 2017, reflecting the decline in global open-ocean CO_2 observation capacity (Bakker et al., 2024). Although recently studies have increasing employed artificial intelligence and big data technologies to investigate the dynamics of ocean carbon sinks (Landschützer et al., 2013; Xu et al., 2019; Yu et al., 2023), the fundamental limitation of in-situ field observation remains unresolved. Due

40 to the limited spatial and temporal coverage of ΔpCO_2 measurements, as well as uncertainties in wind forcing and transport velocity parameterization, the uncertainty in global and regional fluxes estimated from ΔpCO_2 measurements can reach up to ±50% (Wanninkhof et al., 2013; Rhein et al., 2013). In addition to ΔpCO_2 data, air-sea CO_2 fluxes can also be estimated using a top-down inversion method that integrates atmospheric CO_2 concentrations with atmospheric transport models (Jacobson et al., 2007;

45 Wanninkhof et al., 2019). Spatial and temporal variations in atmospheric CO_2 concentrations reflect the pattern of sources and sinks across large spatial scales. Consequently, top-down atmospheric inversion methods are suitable for assessing global and regional CO_2 fluxes and are currently widely adopted to

estimate CO_2 emissions from fossil fuels and carbon sinks in terrestrial ecosystems (Piao et al., 2022;

Han et al., 2024). However, due to the sparse sampling of CO_2 concentration over the open ocean,

50   significant uncertainties persist in those flux estimations, limiting its applicability (Rödenbeck et al.,

2006; Wanninkhof et al., 2019). In summary, the scarcity of marine atmospheric CO_2 concentration

observations is the primary obstacle to accurately quantify the oceanic carbon sink.

   For marine atmosphere, buoy observations excel at meeting the requirements of expanding field

observation coverage and significantly increasing data volume compared to research vessel observations

55   constrained by voyage frequency, range, and cost, or satellite observations limited by operational cycles

and atmospheric conditions (e.g., clouds, aerosols). Currently, both the ARGO Global Ocean Observing

System and the Southern Ocean Carbon and Climate Observation and Modeling (SOCCOM) project

have proposed utilizing buoys for seawater CO_2 observations (Sarmiento et al., 2023), but none of them

have conducted atmospheric CO_2 concentrations over the ocean. Urban CO_2 monitoring efforts provide

60   valuable experience for selecting CO_2 observation instruments suitable for deployment on buoys. In

recently years, high-density monitoring networks based on low-cost CO_2 sensors have been established

in numerous cities worldwide (Karion et al., 2020), as supplements to the land-based observations from

the sites within the World Meteorological Organization's (WMO) Global Atmosphere Watch Programme

(GAW). For instance, Shusterman et al. (2016) established a CO_2 observation network (BEACO$_2$N)

65   which consists of 34 sensors in and around Oakland, California. After applying environmental parameter

and drift corrections, the network achieved an accuracy of $\pm 1.2 - 2.0$ ppm for 1-minute average dry-air

concentrations between, effectively capturing CO_2 variations across multiple temporal scales in urban

areas and abnormal short-term CO_2 emission events. Delaria et al. (2021) further corrected the

temperature-dependent zero bias of the BEACO$_2$N sensor, reducing the error to 1.6 ppm or less. Han et

70   al. (2024) established a 134-station SenseAir K30 sensor observation network and developed a CO_2

calibration system. Data accuracy was enhanced through averaging raw observations, environmental

corrections, and calibration with standard gases. After applying long-term drift correction, the sensors

(SENSE - IAP) maintained a root mean square error (RMSE) of 2.4 ± 0.2 ppm after 30 months of

operation (Cai et al., 2025). Compared to high-precision instruments, low-cost sensors exhibited

75   relatively lower accuracy (several ppm versus ~ 0.1 ppm) but at drastically reduced cost (under 15,000

dollars versus over 150,000 dollars). This cost-performance balance enables the construction of dense

observation networks to reveal significant spatial variations of CO_2 induced by emission sources,

vegetation carbon sinks, and meteorological conditions (Shusterman et al., 2016; Bakker et al., 2024; Han et al., 2024; Cai et al., 2025).

80   Considering the advantages of low-cost sensors in land-based CO_2 monitoring and inversion, and the relative maturity of buoy-based observation technologies, we designed a sea-air interface buoy platform equipped with SenseAir K30 sensors (SenseAir AB, Delsbo, Sweden) in the coastal waters off Maoming, Guangdong, China, and evaluated its performance in monitoring marine atmospheric CO_2 concentration. Satisfying measurement accuracy was obtained after instrumental calibration, data

85   processing, and correction strategies, validating the feasibility of marine CO_2 monitoring with low-cost sensors. Here we presented the preliminary results of the buoy-based low-cost sensor system for atmospheric CO_2 monitoring at the Sea-Air interface. Section 2 introduces the instruments and data correction methods; Section 3 presents the results of the land-based experiments for calibration and correction; and Section 4 demonstrates a short-term marine observation case study.

90   ## 2   Data and Methods

2.1   Instruments and observation site

This study employed a low-cost sensor system integrating three CO_2 Sensor Modules (referred to as CM1, CM2, and CM3) (Figure 1c), capable of simultaneously measuring atmospheric CO_2 concentration and meteorological parameters including temperature, pressure, and humidity. Each CM

95   integrates a CO_2 sensor, environmental parameter sensors, and a Micro-controller Unit (MCU) processor onto a single circuit board housed within a waterproof cube enclosure. Three CM modules are individually mounted in cylindrical housings bolted to a cube enclosure, with silicone seals at the connection points. Both sides and the bottom of the individual housings are wrapped with a membrane that is both breathable and waterproof, ensuring the CMs can operate normally in a marine environment.

100   The CM feature an open-type design that allows ambient air to flow directly through the sensing chamber, without a sealed sampling volume typical of high-precision analysers. The sensors are paired with a data acquisition instrument, and data is collected by a micro-processor named BeagleBone Green Wireless (BBGW) and transmitted back to the server via 4G communication from the base station.

The CO_2 sensor is the K30 sensor module from SenseAir of Sweden, operating on a non-dispersive

105   infrared principle (NDIR). Compared to other low-cost sensors (such as the COZIR Environmental

Sensor (CO$_2$Meter, Inc., Orlando, FL, USA) and TelaireT6615 (Amphenol Advanced Sensors, USA),

etc.), it demonstrates higher raw accuracy, with $\pm$ 30 ppm $\pm$ 3% (Martin et al., 2017), with a

measurement range of 1-10,000 ppm and a resolution of 0.01 ppm, featuring easy configuration and

maintenance-free operation. To account for the influence of external environmental variations on the

110 K30 sensor's response, the CM is equipped with a BME680 sensor (Bosch Sensortec GmbH, Reutlingen,

Germany) that simultaneously monitors temperature (T, °C), relative humidity (RH, %), and atmospheric

pressure (P, hPa) of the internal air mass. The measurement accuracies are $\pm$ 0.1 °C, $\pm$ 3%, and $\pm$ 0.6 hPa,

with corresponding resolutions of 0.01 °C, 0.01%, and 0.01 hPa, respectively. These measurements

enable real-time correction of the CO$_2$ response values for environmental parameters, thereby enhancing

115 the overall accuracy of the observations. The CMs adopt a standard RS485 output mode and are powered

by the buoy's 12 V DC battery, operating continuously with a 2s sampling interval. In the marine

environment, pitching, strong winds, wave impacts, and rainy conditions are common. Combined with

the high humidity and salinity of surface air, these factors often cause condensation and salt deposition

on instrument surfaces. To mitigate these effects, the sensors and data logger were connected and

120 securely mounted inside a Stevenson screen (Figure 1c), which was installed near the buoy's center of

gravity within the supporting frame (Figure 1b), at an approximate height of 3 m above the sea surface,

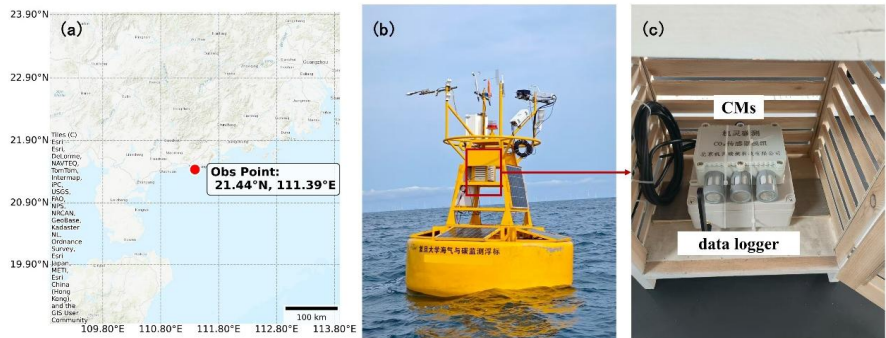to provide a relatively stable observation environment.

Figure 1: Deployment and performance evaluation of buoy-mounted sensors for marine atmospheric CO$_2$
125 **observation. (a) Location of the offshore observation site. Basemap source: Esri World Topographic Map**
(Esri, https://server.arcgisonline.com). (b) On-site scene of the offshore buoy during observation. (c)
Schematic of the CO$_2$ sensor modules (CMs), data logger, and Stevenson screen.

The sea-air coupled monitoring buoy system is composed of a buoy platform and a land-based

station (Figure 2). The buoy consists of a buoy body, mooring system, sensors, data acquisition system,

130 power system, safety system, and communication system. Real-time data transmission between the buoy

and shore station is achieved via BeiDou (Figure 1b). The buoy body has a diameter of 3 meters, a depth

of 0.9 meters, and a total height exceeding 5 meters. The power system comprises high-capacity, compact,

rechargeable batteries, and solar panels. The batteries are housed within the instrument compartment,

while solar panels are mounted around the buoy tower. These panels charge the batteries, supplying a

135 single operating voltage to the buoy system. The system can sustain normal power supply to the buoy

observation system for 15 consecutive days of overcast or rainy weather, ensuring continuous and reliable

operation even under severe sea conditions. The buoy data communication system employs dual-mode

Beidou and Iridium satellite communication, with redundant data transmission to ensure an effective data

reception rate of better than 95%. The shore station reception and processing system features reception,

140 post-processing, and report generation capabilities, enabling modification and configuration of

parameters such as buoy sampling frequency and transmission cycle. It also provides low-voltage, water

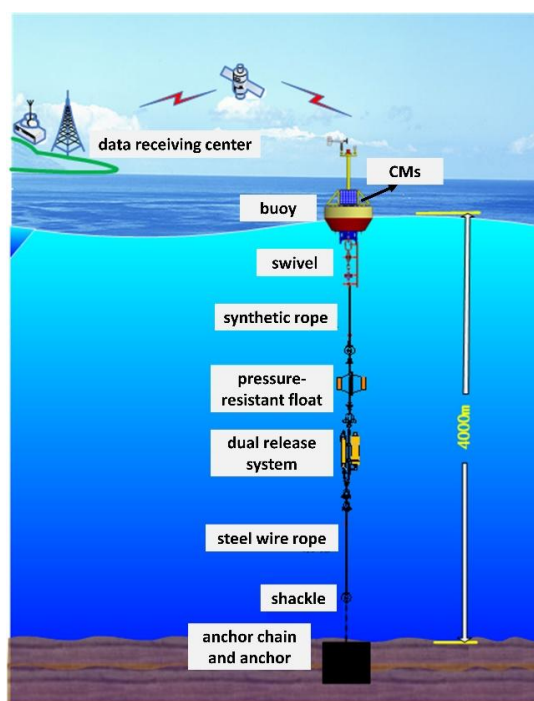ingress, and displacement alarm functions for buoys.

Figure 2: Schematic diagram of a deep-sea air-sea coupled monitoring buoy system

145   To calibrate the CMs, it was first placed in the laboratory and a meteorological observation field

within Jiangwan Campus of Fudan University, for side-by-side observations with a cavity ring-down

spectrometer (Picarro G2301, Picarro Inc., Santa Clara, USA). (Figure 3). The CMs equipped with

Stevenson screen was placed outside the station building, while the sampling gas tube of Picarro was

extended into the Stevenson screen through a duct connecting the station building to the outside

150   environment, ensuring simultaneous observations with CMs. Following land-based field observations,

the instrument was deployed for field observations at sea. The offshore field observation point is located

in the coastal area of Dianbai District, Maoming City, Guangdong Province (21.44 °N, 111.39 °E)

(Figure 1a), belonging to northern shelf coastal section of the South China Sea nearshore areas feature

port zones, shallow bays, and small islands (such as Dazhuzhou), while offshore lies the broad continental

155   shelf and slope transition zone of the northern South China Sea. Integrated multi-source observations

indicate that most of the South China Sea is a weak to moderate CO_2 source with seasonal variations

(Zhai et al., 2013; Li et al., 2020; Chen et al., 2024; Zhang et al., 2024). The annual average flux in the

northern continental slope region is approximately 0.46 mol m^{-2} yr^{-1}, with higher values in the central

and southern areas (about 1.37 mol m^{-2} yr^{-1}) (Zhai et al., 2013). During summer, the coastal upwelling

160   brings up subsurface water rich in dissolved inorganic carbon and low in temperature to the surface layer,

typically tending to increase atmospheric CO_2 emissions. However, spatiotemporal variations in wind

events, biological consumption, and estuarine runoff can cause significant short-term or inter seasonal

reversals (Xu et al., 2013; Li et al., 2021). In summary, the northern South China Sea, where the

observation point in this study are located, is generally characterized as a minor CO_2 source but exhibits

165   strong spatiotemporal variability (Zhang et al., 2024).
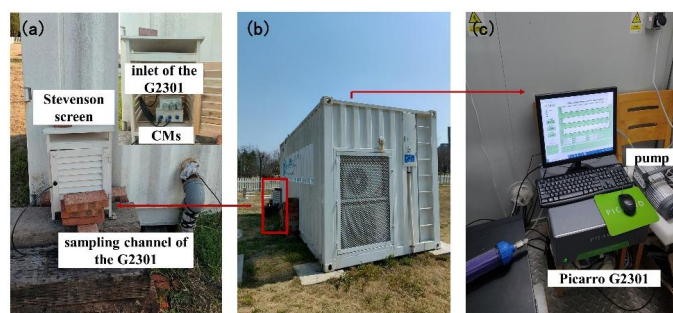

Figure 3: Land-based field observation experiments. (a) Configuration of CMs, Stevenson screen, and Picarro sampling channel. (b) Meteorological observation station, experimental cabin, and field deployment of CMs. (c) Field setup of the Picarro G2301.

170 **2.2 CMs data correction method**

The original signals had a sampling interval of 2 s and a background noise level of ± 30 ppm. The raw data from the CMs were filtered and resampled. After quality control, outliers deviating by more than 4σ from the mean were removed, and temporal averaging was applied to reduce the noise level. The 4σ threshold is applied to achieve a compromise between eliminating extreme outliers and retaining the

175 inherent variability of the dataset (Cai et al., 2025). Allan variance, which quantifies the time-averaged stability of continuous measurements, was used to determine the optimal averaging interval that minimizes noise while preserving the integrity of the data signals (Martin et al., 2017). Langridge (2008) indicated that the optimal averaging time for the Allan variance of the K30 sensor to reach its minimum is approximately 3 min, after which extending the averaging time step no longer significantly reduces

180 the noise. Cai et al. (2025) evaluated the noise characteristics of the SenseAir K30 by continuously introducing standard gases. The results showed that at a measurement interval of 2 s, the noise level was 4 ppm, and 1-2 min showed 0.4-0.7 ppm noise level, and from 2 min to 1 h, the noise level decreased to approximately 0.2 ppm. Therefore, in this study, we selected a 1-minute time step to average the raw data before proceeding with subsequent corrections. This approach significantly reduces the noise level

185 in the data while enabling the resolution of atmospheric changes on a relatively short timescale.

Using CM1 as an example, results from observations conducted by CMs and Picarro in laboratory and terrestrial field are presented in Figure 4. After quality control and resampling of raw data, the standard deviation (SD) for the three CMs in laboratory tests improved from 13.05, 17.32, 18.28 ppm to 4.68, 5.26, and 5.48 ppm, respectively. For field tests, the values improved from 15.14, 21.93, 17.06 ppm

190 to 9.33, 14.83, and 8.83 ppm, respectively (Figure 4; Figures S1-S2). Data accuracy improved after minute averaging (Figure 4 a-d), but differences still exist compared to the reference instrument Picarro (ΔCO_2). A comparison between the laboratory and field results (Figure 4 c, d) shows that the CMs performed better under laboratory conditions. In the stable laboratory environment, ΔCO_2 exhibited no pronounced diurnal variation (Figure 4 c, e), fluctuating steadily around a constant value (system bias).

195 By contrast, in the field, where atmospheric conditions naturally vary (Figure 4f), the environmental parameters showed clear diurnal cycles, and ΔCO_2 also displayed diurnal oscillations. This indicates that the CMs are highly sensitive to environmental conditions, and their measurement accuracy is affected by both atmospheric variability and the CO_2 concentration baseline. Therefore, further calibration with

respect to environmental parameters is required. The most used environmental correction method for

200   NDIR sensors is multiple linear regression. This involves establishing empirical regression models using

environmental parameters such as temperature, air pressure, and water vapor under laboratory or side-

by-side observations with standard instrument (Martin et al., 2017; Han et al., 2024; Cai et al., 2025). In

recent years, numerous studies have attempted to model environmental nonlinear effects using machine

learning methods such as random forests, gradient boosting, or neural networks, achieving lower root

205   mean square error (RMSE) than linear regression (Biagi et al., 2024; Dubey et al., 2024). However, these

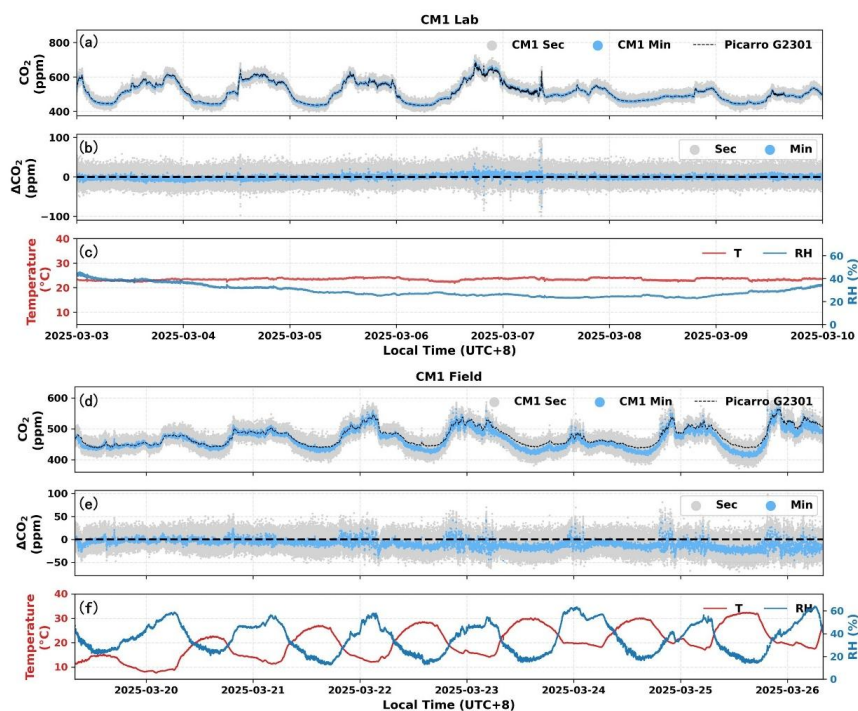approaches still exhibit limitations in interpretability and transferability.

Figure 4: Time series of CM1 data during laboratory (a, c, e) and land-based field (b, d, f) observations. (a, d) CM1-measured CO$_2$ concentration at second-level resolution (grey dots) and minute-level resolution (blue dots), alongside Picarro-measured CO$_2$ concentration (black line). (b, e) Time series of CO$_2$ concentration difference (ΔCO$_2$=CM1-Picarro) at second-level (grey dots) and minute-level (blue dots) resolution. (c, f) Time series of ambient temperature (T, red line) and relative humidity (RH, blue line).

The 1-min ΔCO$_2$ exhibits linear relationships with *T*, *P*, and *RH*, and this environment-related

dependence differs among individual CMs (Figure 5). Based on these characteristics, this study adopts a

215   multiple linear regression approach for environmental calibration as Cai et al., (2025), where ΔCO_2 and

the environmental parameters satisfy the following relationship:

$$\Delta C = Y_{CM} - y_0 \qquad (1)$$

$$\Delta C = a_0 + f(a_t, T) + f(a_p, P) + f(a_{RH}, RH) + f(a_c, CO_2) \qquad (2)$$

Here, Y_{CM} represents the CMs measurements, and y_0 is the true atmospheric CO_2 concentration.

The coefficients a_t, a_p, a_{RH}, and a_c are the correction parameters associated with T, P, RH, and the CO_2

concentration, respectively; including the CO_2 term in the calibration equation serves to eliminate the

220   zero-point bias of the CMs. For each CM, the corresponding values of a_t, a_p, a_{RH}, and a_c are unique.

a_0 is the baseline concentration correction parameter, calibrated using measurements from reference

instruments at the observation site or from nearby atmospheric background stations. All these parameters

can be determined through multiple linear regression using the `Linear Regression` function in Python.

The corrected data of CO_2 after environmental correction is:

$$y_{corrected} = Y_{cm} - a_0 - f(a_t, T) - f(a_p, P) - f(a_{RH}, RH) - f(a_c, CO_2) \qquad (3)$$

225   When standard instrument (e.g., Picarro) co-located observations are available, these measurements

shall be considered the true values for atmospheric CO_2 concentrations. The specific correction results

will be described in Section 3. For marine observations, the baseline correction of CMs is performed

using data from the Mauna Loa atmospheric background station in Hawaii, USA (Thoning et al., 2025),

corresponding to periods where CMs observations are stable and close to background values. The specific

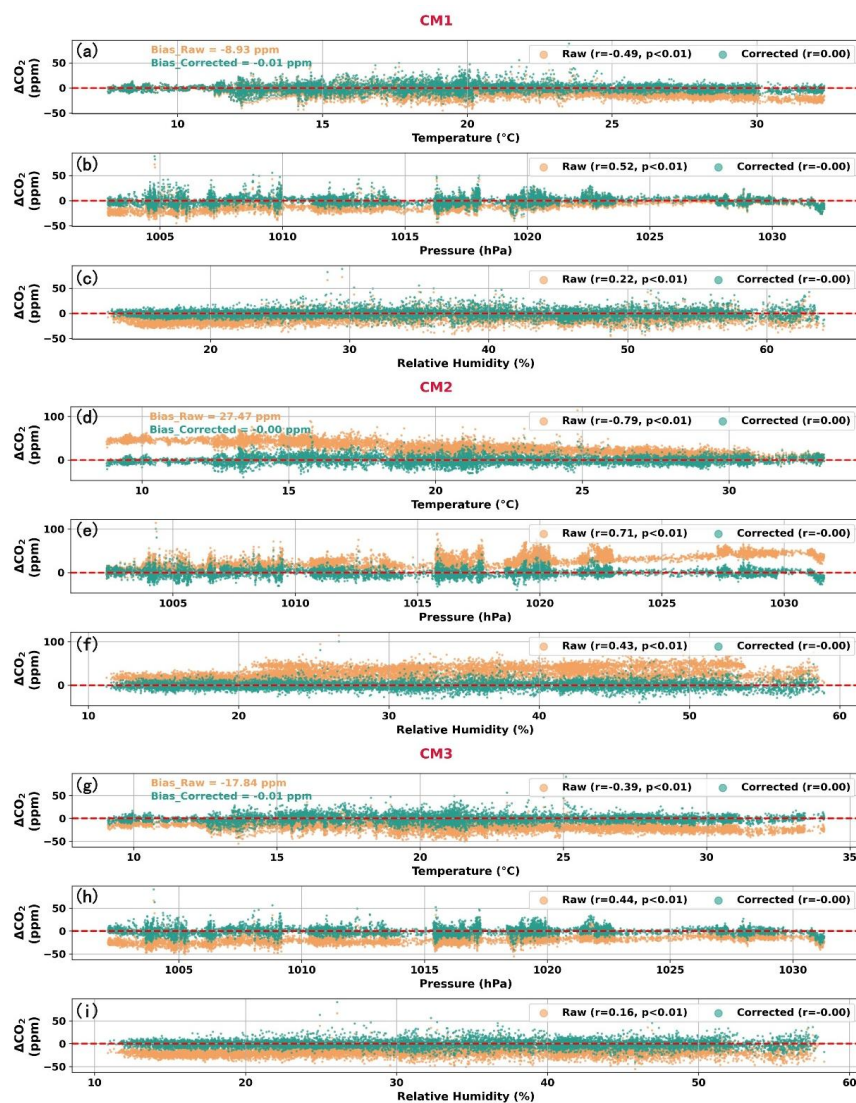230   method and results will be introduced in Section 4.

3   Environmental correction results for land-based field observations

Temperature variations affect the sensor's light source intensity, detector response, and absorption

cross-section, leading to systematic drifts in output (Yasuda et al., 2012). Pressure influences gas density

and infrared absorption line broadening, making corrections based on the equation of state or sensor

235   sensitivity particularly important in regions with strong pressure fluctuations (Chen et al., 2010; Curcoll

et al., 2022). Water vapor exerts the most complex effects on NDIR sensors: it not only dilutes CO_2 mole

fractions in moist air relative to dry air but also causes spectral line broadening within the CO_2 absorption

band, introducing biases (Chen et al., 2010; Dubey et al., 2024). Accordingly, the multivariate linear

calibration of CMs focuses on three key environmental factors - T, P, and RH. Figure 5 shows the

240   variations of ΔCO_2 between the three CMs and the collocated Picarro measurements as a function of

environmental parameters (T, P, and RH) during the land-based field observations, where the orange and

green colors correspond to the data before and after environmental correction, respectively. Figure 6

presents the linear relationships between the CMs and the Picarro, along with the histograms of ΔCO_2.

Prior to correction, the ΔCO_2 of all three CMs exhibited linear relationships with environmental

245   parameters (Figure 5): negative correlation with T, and positive correlation with P and RH. Among these,

CM2 demonstrated the most pronounced correlations. The correlation coefficients (r) between ΔCO_2

and T, P, and RH were -0.79, 0.71, and 0.43, respectively, while the r values for CM1 and CM3 were -

0.49, 0.52, 0.22, and - 0.39, 0.44, 0.16, respectively, all significant at the 0.01 level ($p < 0.01$). After

correction, the systematic drift of ΔCO_2 across the three CMs due to environmental parameters was

250   successfully eliminated. The corresponding r values were all 0, indicating no significant correlations,

with ΔCO_2 fluctuating around the zero line. Beyond environmental factors, the multiple linear

regression also incorporated the true CO_2 concentration in the atmosphere, represented by Picarro co-

located measurements in field observations. The values of the first three CMs before correction all exhibit

zero bias relative to the true values (the fit between CO_2 observations and true values includes intercepts)

255   (Figure 6 a-c), with respective r values of 0.98, 0.93, and 0.98, all significant at the 0.01 level ($p < 0.01$).

After correction, the correlations all improved to 0.99 ($p < 0.01$), and data points largely converged on

either side of the 1:1 line. The bias between CMs and Picarro shifted from -3.7 ppm, + 43.6 ppm, and -

16 ppm to + 0.1 ppm, + 1.6 ppm, and + 0.6 ppm, respectively, shifting from significantly biased to

essentially unbiased (Figure 6 d-f). The results above suggest that all three CMs are influenced by

260   environmental variables, but to markedly different extents. Whether for CM2, which inherently exhibits

substantial systematic errors, or CM1, which shows minimal data offset prior to correction, our

environmental correction method significantly enhances observational accuracy, improves data quality,

and demonstrates good universality.

Figure 5: Variations of ΔCO_2 (ΔCO_2=CM-Picarro) for CM1 (a-c), CM2 (d-f), and CM3 (g-i) during land-based field observations, as functions of temperature (a, d, g), atmospheric pressure (b, e, h), and relative humidity (c, f, i). Orange dots represent data before environmental correction, while green dots represent data after environmental correction.
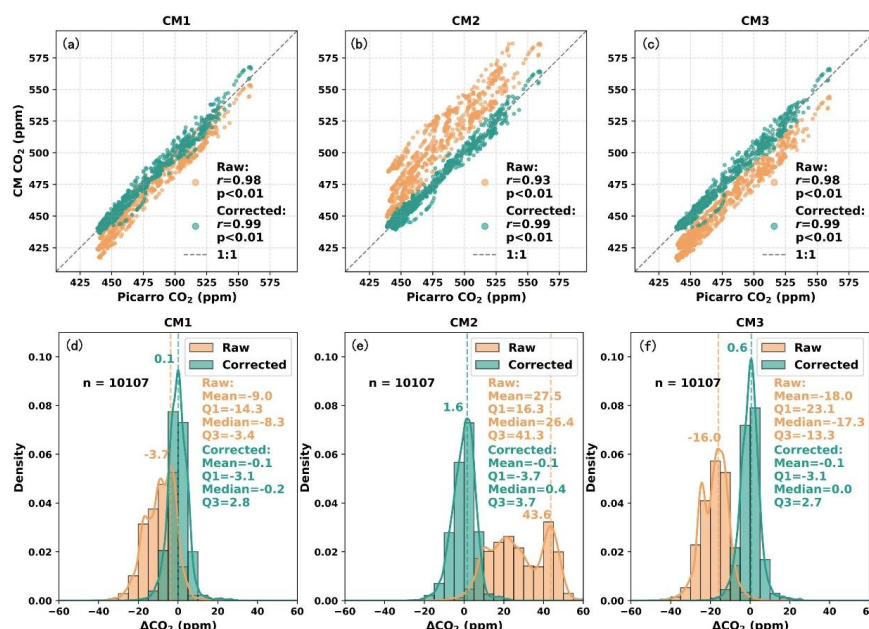
Figure 6: Direct comparison of hourly moving averages of CO_2 concentrations among CM1, CM2, CM3 and Picarro during land-based field observations (a-c), and histograms of ΔCO_2 distributions (d-f) (ΔCO_2=CM-Picarro, where CM corresponds to CM1, CM2, and CM3, respectively). Orange dots and bars represent data before environmental correction, while green dots and bars represent data after environmental correction.

Environmental correction effectively reduced the offset values between CMs and Picarro (Figure 7). Before correction, CMs captured CO_2 concentration trends like Picarro but exhibited significant deviations. For the best performing CM1, this deviation was particularly noticeable at low CO_2 concentrations, while CM2 and CM3 showed overall high and low biases, respectively. The ΔCO_2 of CMs exhibited a certain "downward" drift trend over the one-week observation period, CM1 and CM3 moved from zero toward negative values, while CM2 shifted from a relatively high positive value around 50 ppm toward zero. The calibrated results showed high consistency with Picarro, with the RMSE decreasing from 11.04 ppm, 30.51 ppm, and 18.70 ppm to 4.03 ppm, 3.96 ppm, and 3.88 ppm, respectively. The correction effectively eliminated the linear drift trend of ΔCO_2 over time, stabilizing it to fluctuate around the zero line. During the land-based field observations in Shanghai in early spring, the atmospheric temperature and humidity exhibited pronounced diurnal variations, fluctuating between 5-30 ℃ and 10-60%, respectively. The average RMSE of corrected CMs was 3.64 ppm, which is sufficient to capture terrestrial CO_2 variations (400-600 ppm), even during periods of significant CO_2

fluctuations with pronounced peaks and troughs, such as cases on March 22nd-23rd and March 25th-26th, where the environmental correction method performed well.
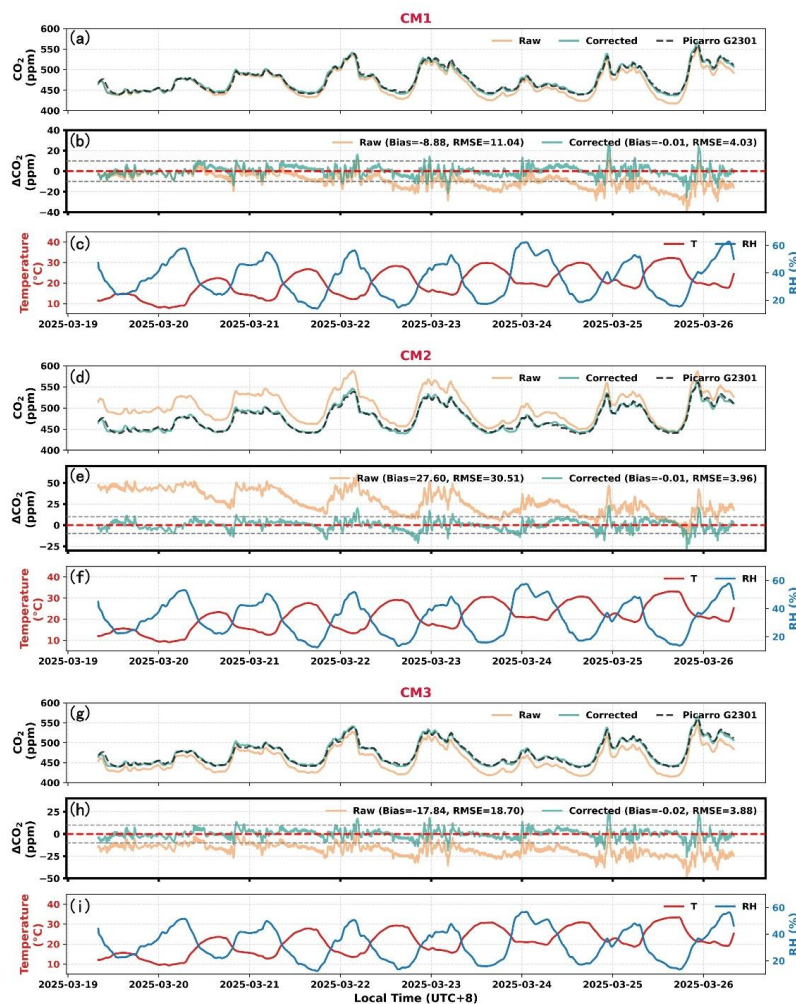

Figure 7: Hourly moving average time series of CM1 (a-c), CM2 (d-f), and CM3 (g-i) during land-based field observations: CO$_2$ concentration of CMs before environmental correction (orange line), after environmental correction (green line) , and CO$_2$ concentration from Picarro (black dashed line) (a, d, g); ΔCO$_2$ (ΔCO$_2$=CM-Picarro) of CMs before and after calibration (b, e, h); Ambient temperature (T, red line) and relative humidity (RH, blue line) (c, f, i).

4   Marine observation results

Based on the instrument deployment and marine environment described in Section 2, and the environmental correction method validated through land-based field observations in Section 3, the CMs-

equipped air-sea interface buoy observation platform commenced operation in May 2025 in the northern

South China Sea off the coast of Dianbai District, Guangdong Province. Following signal debugging and

300   regular equipment maintenance, observational data were obtained over three months from May 28th to

August 28th. The hourly moving-averaged time series of CO_2 concentration, T, and RH from the three

CMs are shown in Figure 8. During environmental calibration, measurements are first corrected using

the environmental coefficients a_t, a_p, a_{RH}, and a_c obtained from land-based calibration; baseline

correction is then applied by updating a_0 with reference CO_2 concentrations from the marine

305   atmospheric boundary layer. Over the open ocean, strong horizontal atmospheric mixing results in small

zonal variations in marine boundary layer CO_2 concentrations, indicating high zonal uniformity at similar

latitudes (Bakwin et al., 2004; Palter et al., 2023). Given the strong real-time nature of this study's

observations and the limited availability of co-located and near-surface observation resources, CO_2

observation data from the Mauna Loa atmospheric background station in Hawaii, USA (MLO, 19.54°N,

310   155.58°W) - located at a latitude similar to the observation site - served as the reference value. The CO_2

datasets   were   obtained   from   the   NOAA   Global   Monitoring   Laboratory   (GML)

(https://gml.noaa.gov/ccgg/trends/data.html; Thoning et al., 2025). The relatively stable period (June

17th-24th) of CMs concentrations during the observation was regarded as the atmospheric background

state. Both values were substituted into a multiple linear regression calculation to obtain a_0. After

315   environmental correction, the RMSE of the CMs significantly decreased from 9.27 ppm, 52.39 ppm, and

11.24 ppm to 1.57 ppm, 1.86 ppm, and 1.52 ppm, respectively (Figure 8a; Figures S3-S5).

During the three-month marine observations, the atmosphere at the observation site exhibited high

temperatures and humidity, with temperatures ranging from 25 to 37.5 °C and humidity levels between

50% and 100% (Figure 8b). Both showed pronounced diurnal and weekly variations. The mean CMs

320   values before and after correction were 459.48 ppm and 436.94 ppm, with medians of 456.53 ppm and

433.75 ppm, respectively (Figure 8c). The means consistently exceeded the medians, and the ranges

surpassed 100 ppm in both cases, which indicates many signal peaks in CO_2 during the observation, and

the observation site is susceptible to terrestrial anthropogenic CO_2 emissions. After correction, the overall

concentration was approximately 22 ppm lower than the original values, consistent with the CO_2 range

325   at the atmospheric background station MLO (mean 429.32 ppm). The correction eliminated systematic

overestimation, bringing the results closer to background concentrations.

The SD of the raw data is 9.79 ppm, showing a slight difference from the corrected value of 9.62

ppm. The first quartile (Q1) changed from 453.08 ppm to 430.10 ppm, and the third quartile (Q3) changed

from 463.29 ppm to 441.32 ppm, with an inter-quartile range (IQR) of 10.21 ppm, slightly below the

330   corrected value of 11.22 ppm. These indicate that the correction process reduced the overall CO_2

concentrations but did not significantly decrease data variability. In fact, the distribution of the middle

50% of data points became wider. Whether considering the extreme fluctuation range (extreme value

difference) influenced by anthropogenic land effects, the typical fluctuation range IQR after removing

most extreme signals, or the average fluctuation amplitude SD of overall concentrations, the accuracy of

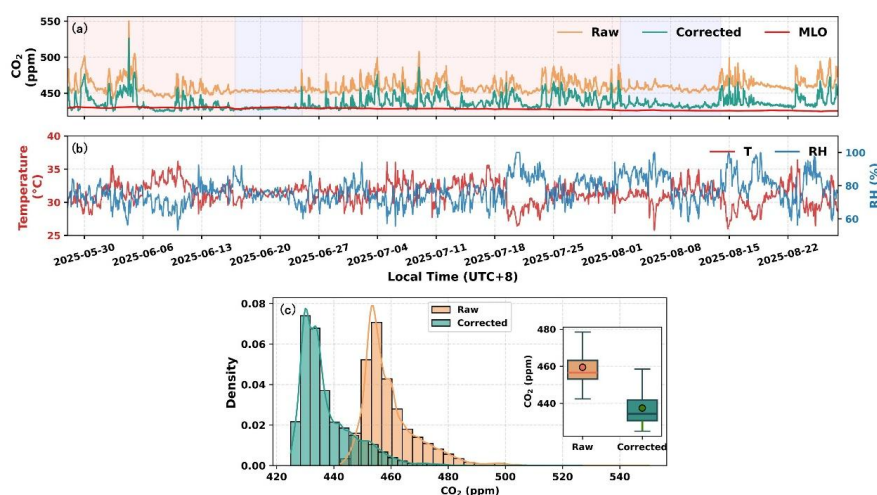335   CMs corrected data is sufficiently to capture the corresponding signals.

Figure 8: Offshore buoy observation results of CMs. (a) Hourly moving average time series of CO_2
concentrations from CMs before correction (orange line) and after correction (green line), together with daily
mean CO_2 series from Mauna Loa Observatory (MLO, red line). The light red and light blue shaded
340   **backgrounds correspond to CO_2 fluctuation periods and stable periods, respectively. (b) Time series of**
ambient temperature (T, red line) and relative humidity (RH, blue line). (c) Histograms and boxplots showing
the distributions of CO_2 concentrations before (orange bars) and after correction (green bars).

During the three-month observation period, CO_2 at the monitoring site exhibited short-term

fluctuation peaks as well as periods of stable concentrations, both of which can be analyzed and

345   interpreted from the perspective of atmospheric transport. Using the NOAA Hybrid Single-Particle

Lagrangian Integrated Trajectory (HYSPLIT) model, 36-hour backward trajectories were calculated for

the observation point to identify the primary transport pathways influencing the air mass sources at the

location (Cohen et al., 2015). The trajectory origin is set at the observation point, with a time resolution of 6 hours. Meteorological driving data were from the Global Data Assimilation System (GDAS1, 1° × 1°) reanalysis data provided by NOAA (Rolph et al., 2017). After obtaining a series of backward trajectories, the HYSPLIT clustering module was employed to classify the trajectories. This approach mitigates the impact of uncertainty inherent in individual trajectories and extracts key transport pathway characteristics, providing a basis for subsequent analysis of the relationship between air mass transport and observational results (Cohen et al., 2015). The entire period of marine observations was divided into four segments for clustering. The periods from May 28th to June 16th (Figure 9a) and June 25th to August 1st (Figure 9c) constituted CO_2 fluctuation phases (the background is light red in Figure 8a), with many concentration peaks occurring during these periods. The periods from June 17th to 24th (Figure 9b) and August 2nd to 13rd (Figure 9d) constituted CO_2 stable phases (the background is light blue in Figure 8a). During these phases, CO_2 concentrations fluctuated minimally and approached the background levels of the marine boundary layer. It is particularly noteworthy that during the two-week period from August 14th to August 28th (the background is white in Figure 8a), CO_2 exhibited alternating patterns of relatively dense peaks and sustained background concentration levels, with each state lasting no more than five days. The limited number of trajectories obtained from segmented analysis makes it inconvenient for cluster analysis.

The trajectory clustering results (Figure 9) indicate that the atmospheric transport pathways corresponding to concentration fluctuation periods are relatively complex, significantly influenced by air masses transported from land. Trajectories from May 28th to June 16th were classified into 17 categories, with 40% originating from land and 60% from the ocean. The most typical inland air mass, represented by Trajectory 4, was transported from northern Guangdong all the way to western Guangdong. Trajectory 12, although originating from the sea, reached the observation point via the western coast of Guangdong within the first 6 hours of the observation period. From June 25th to August 1st, trajectories ending over land accounted for 54%, while those ending over the ocean accounted for 46%. Trajectory 2, corresponding to short-range inland transport, accounted for 13%. The clustering results indicate that local urban emissions from land areas significantly contributed to CO_2 concentrations at the observation point, effectively explaining the observed large fluctuations and multiple peaks during the corresponding period. Correspondingly, air masses at observation point during concentration stable periods were predominantly transported from clean marine atmospheres. The trajectories from June 17th to 24th were

18

clustered into 11 groups, all originating from the South China Sea. Consequently, the observed CO_2

concentrations during this period remained near background levels, which can be considered the CO_2

380 concentration level in clean air without anthropogenic pollution. This also demonstrates that using CO_2

observations from this period combined with MLO atmospheric background concentrations for baseline

correction of CMs is reasonable. Trajectories from August 2nd to 13rd were categorized into 4 types,

with 92% originating from marine sources and 8% from land sources. Consequently, although CO_2

concentrations at observation point during this period were slightly elevated above background values,
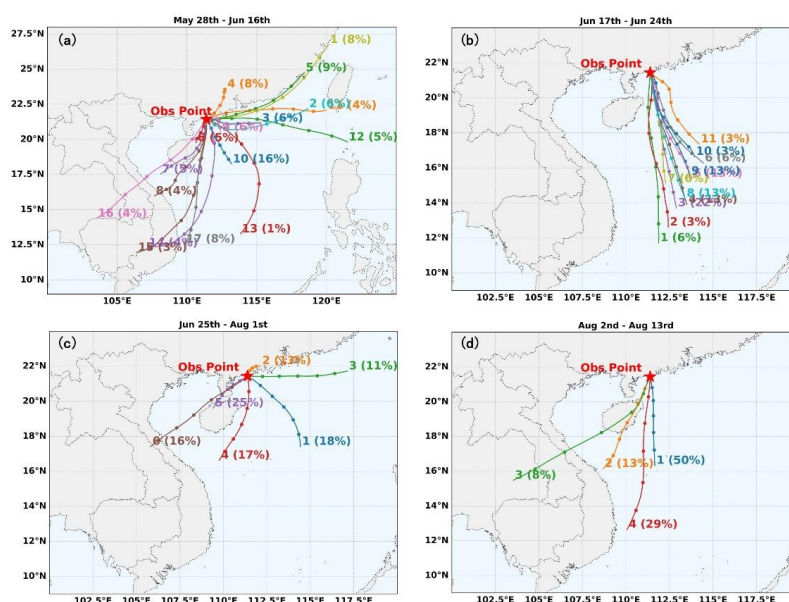
385 they remained generally stable.

Figure 9: Clustered results of 36-hour backward trajectories from Hybrid Single-Particle Lagrangian Integrated Trajectory (HYSPLIT) model analyses at the offshore observation site during four time periods of buoy observations. Each trajectory is labeled with its cluster number and proportion, and markers on the
390 **trajectories indicate 12-hour intervals. (a) 28th May-16th June, (b) 17th-24th June, (c) 25th June-1st August, (d) 2nd-13rd August. (a) and (c) correspond to CO_2 concentration fluctuation periods, while (b) and (d) correspond to CO_2 concentration stable periods.**
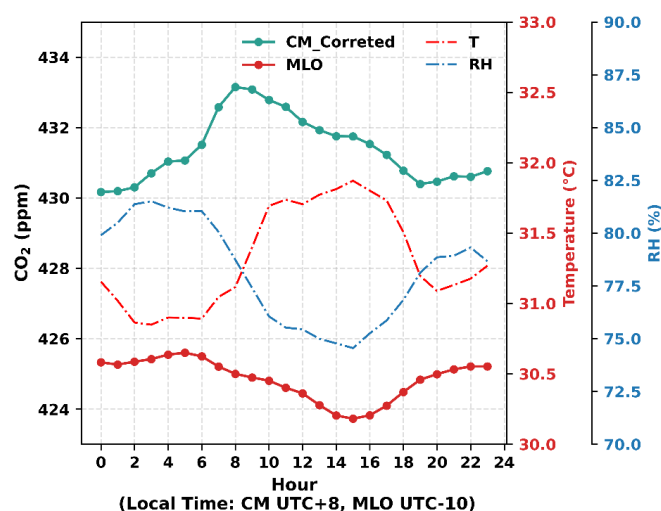
By comparing the corrected CMs data during the concentration stable periods (including 19

complete days) with the diurnal variations in CO_2 concentration during the summer of 2024 (June to

395 August) at the MLO station (Figure 10), we can further understand how CMs captures the diurnal

variation of oceanic boundary layer CO_2. Hourly CO_2 mole fractions at MLO were obtained from NOAA

GML (https://gml.noaa.gov/data/dataset.php?item=mlo-co2-observatory-hourly; Thoning et al., 2025).

19

Both CMs and MLO exhibit daily variations in background CO_2 concentrations characterized by lower daytime values and higher nighttime values. This pattern likely stems from the primary influence of air-

400   sea CO_2 fluxes and atmospheric convective transport on oceanic CO_2 concentrations (Lv et al., 2015). During the day, solar radiation heats the Earth's surface, which enhances photosynthesis in marine ecosystems and promotes the uptake of atmospheric CO_2. As atmospheric temperatures rise, enhanced turbulent activity thickens the mixed layer, diluting CO_2 through vertical mixing and reducing its concentration. At night, photosynthesis ceases in regional marine ecosystems, leaving only respiration.

405   The sea surface cools, and weakened turbulent mixing restricts vertical air exchange.CO_2 struggles to diffuse into the upper layers, accumulating in the near-surface layer and increasing in concentration. The daily amplitude of CO_2 at MLO station during summer is approximately 2 ppm, while CMs is 3 ppm. This indicates that the environmentally calibrated CMs is sufficiently sensitive to capture the daily variation signal of CO_2 in clean background air unaffected by terrestrial anthropogenic emissions,

410   demonstrating its potential for observing atmospheric CO_2 concentrations in open ocean environments. The daily amplitude of CO_2 at MLO Station during summer is approximately 2 ppm, while CMs is 3 ppm. This indicates that the environmentally calibrated CMs is sufficiently sensitive to capture the daily variation signal of CO_2 in clean background air unaffected by terrestrial anthropogenic emissions, demonstrating its potential for observing atmospheric CO_2 concentrations in open ocean environments.

415   Observations of the CMs show that the daily maximum and minimum values of CO_2 exhibit a 3-hour lag compared to the MLO station, which may be attributed to differences in the surrounding environments of the two sites. The MLO station is situated on high altitude land, exhibiting a typical mountainous diurnal variation in CO_2 concentration. Mountainous terrain induces strong upslope and downslope airflows, leading to earlier atmospheric mixing. During the day, upslope flow and mixing

420   intensify (NOAA GML, 2024a), resulting in the lowest concentrations around 4 p.m. when vertical mixing is strongest. At night, the mountain air becomes isolated from the free atmosphere, with downslope flows carrying high CO_2 air (NOAA GML, 2024a), reaching peak concentrations around 6 a.m. The observation site in this study is over an ocean surface, which possesses high thermal capacity, exhibits small diurnal temperature variations, and experiences delayed turbulence enhancement and

425   boundary layer development (Nemoto et al., 2009). Consequently, the nocturnal accumulation of CO_2 persists until 8 a.m., several hours after sunrise. Daytime sea breezes and mixing intensify later, with the lowest CO_2 values occurring around 7 p.m. The average CO_2 concentrations at MLO and CMs were

424.85 ppm and 431.38 ppm, respectively, differing by approximately 6.5 ppm. This discrepancy may

be due to the fact that the comparison uses 2024 data. According to the NOAA, the annual growth rates

430 of CO_2 concentrations for MLO 2023 and 2024 were 3.36 ppm/yr and 3.33 ppm/yr (NOAA GML, 2024b).

Furthermore, even after filtering out short term terrestrial sources, the East Asian monsoon transport can

still cause regional increases in atmospheric CO_2. This monsoon-driven transport represents mesoscale

or large-scale processes, not local pollution peaks, and thus systematic differences between CO_2

concentrations and MLO can still be observed during stable periods (Fang et al., 2014; Lin et al., 2018).

Figure 10: Diurnal variations of CO_2 concentrations from CMs (environmentally corrected, green line) during stable concentration periods and from Mauna Loa Observatory (MLO, Jun-Aug 2024, red line), along with corresponding temperature (T, red dash line) and relative humidity (RH, blue dash line) variations.

5   Conclusions

440   We successfully established a sea-air interface buoy platform along the coast of Maoming,

Guangdong Province, employing low-cost sensors to observe marine CO_2 concentrations in the nearshore

region of the northern South China Sea. Environmental correction methods effectively eliminated the

impact of environmental factors such as temperature, pressure, and humidity fluctuations on CO_2

measurements while correcting for zero bias. With land-based Picarro G2301 co-located observations

445 for comparison, CO_2 accuracy improved from 8.03 ppm to 3.64 ppm. Over ocean, baseline correction

using MLO atmospheric background station data improved accuracy from 24.26 ppm to 1.59 ppm,

meeting the precision requirements for capturing marine CO_2 concentration signals (e.g., 420-480 ppm).

Systematic errors were eliminated, ensuring observed overall concentration levels align with MLO background stations, thereby meeting CO_2 concentration levels in the marine boundary layer. The

450 temporal variations in CO_2 observed by the CMs, including both fluctuating and steady-state phases, can be explained by the long-range atmospheric transport simulated by HYSPLIT. Moreover, the CMs successfully captured the diurnal variations of background CO_2 in the marine atmospheric boundary layer, with an amplitude of approximately 3 ppm.

In summary, this study proposes an environmental correction method for calibrating low-cost

455 sensors, demonstrating its reliability and scientific validity. It has successfully facilitated the application of low-cost sensors aboard buoys for observing marine atmospheric CO_2 concentrations, providing valuable experience for field deployment of marine atmospheric CO_2 monitoring. To our knowledge, this marks the first application of this method, holding significant importance for acquiring CO_2 concentration data in under-observed marine regions. This approach significantly reduces the cost of observing CO_2 in

460 the ocean, opening new possibilities for achieving the goal of substantially increasing observation data. At the same time, high-precision instruments demand stringent environmental conditions. When deployed on buoy platforms in the harsh field observation environment of the ocean, with its powerful winds and waves, maintenance becomes extremely difficult. Low-cost sensors, however, overcome these technical challenges to a large extent.

465 This study represents the first trial in deploying low-cost sensors aboard buoys to monitor marine CO_2 concentrations. The buoy platform equipped with CMs has withstood several typhoon events, demonstrating excellent watertightness, mechanical robustness, and stability under wave conditions, which are essential for reliable long-term marine monitoring. The successful detection of daily variations in the CO_2 stable periods further demonstrates the method's potential for deployment in open ocean

470 observations. To achieve the goal of significantly increasing the number of marine observations, low-cost sensors must be deployed on small drifting buoys in the following studies. Additionally, the data in this paper covers a relatively short time scale and has not yet accounted for long-term sensor drift. As the duration of observations continues to increase, it will be necessary to correct for this long-term drift. Therefore, this method requires continued refinement and enhancement. In the future, if large-scale

475 deployment of buoys for observation can be realized to obtain extensive regional oceanic CO_2 observational data, these data could be utilized for "top-down" atmospheric inversions. This would provide new perspectives and methodologies for estimating air-sea CO_2 fluxes, representing a

groundbreaking endeavor. It holds significant importance for accurately estimating oceanic carbon sinks

and quantifying the dynamics of the carbon cycle.

480

References

Bakker, D. C. E., Alin, S. R., Bates, N. R., Becker, M., Gkritzalis, T., Jones, S. D., Kozyr, A., Lauvset,
495 S. K., Metzl, N., Nakaoka, S.-i., O'Brien, K., Olsen, A., Pierrot, D., Steinhoff, T., Sutton, A., Takao, S.,
Tilbrook, B., Wada, C., and Wanninkhof, R.: SOCAT version 2024: Ocean CO2 observing effort down
to levels of a decade ago, 2024.
Bakwin, P. S., Davis, K. J., Yi, C., Wofsy, S. C., Munger, J. W., Haszpra, L., and Barcza, Z.: Regional
carbon dioxide fluxes from mixing ratio data, 56, 301–311, 10.3402/tellusb.v56i4.16446, 2004.
500 Biagi, R., Ferrari, M., Venturi, S., Sacco, M., Montegrossi, G., and Tassi, F.: Development and machine
learning-based calibration of low-cost multiparametric stations for the measurement of CO(2) and CH(4)
in air, Heliyon, 10, e29772, 10.1016/j.heliyon.2024.e29772, 2024.
Cai, Q., Zeng, N., Yang, X., Xu, C., Wang, Z., and Han, P.: A 30-month field evaluation of low-cost
CO2 sensors using a reference instrument, Atmospheric Measurement Techniques, 18, 4871–4884,
505 10.5194/amt-18-4871-2025, 2025.
Chen, H., Winderlich, J., Gerbig, C., Hoefer, A., Rella, C. W., Crosson, E. R., Van Pelt, A. D., Steinbach,
J., Kolle, O., Beck, V., Daube, B. C., Gottlieb, E. W., Chow, V. Y., Santoni, G. W., and Wofsy, S. C.:
High-accuracy continuous airborne measurements of greenhouse gases CO2 and CH4 using the cavity
ring-down spectroscopy (CRDS) technique, Atmos. Meas. Tech., 3, 375–386, 10.5194/amt-3-375-2010,
510 2010.
Chen, Y., Zhao, H., and Gao, H.: Spatiotemporal Evolution of Air–Sea CO2 Flux in the South China Sea
and Its Response to Environmental Factors, Remote Sensing, 16, 10.3390/rs16244724, 2024.

Cohen, M. D., Stunder, B. J. B., Rolph, G. D., Draxler, R. R., Stein, A. F., and Ngan, F.: NOAA's HYSPLIT Atmospheric Transport and Dispersion Modeling System, Bulletin of the American
515   Meteorological Society, 96, 2059–2077, 10.1175/bams-d-14-00110.1, 2015.

Costa, M. H., Cunha, L. C. d., Cox, P. M., Eliseev, A. V., Henson, S., Ishii, M., Jaccard, S., Koven, C., Lohila, A., Patra, P. K., Piao, S., Rogelj, J., Syampungani, S., Zaehle, S., and Zickfeld, K.: Global Carbon and Other Biogeochemical Cycles and Feedbacks, in: Climate Change 2021 – The Physical Science Basis, 673–816, 10.1017/9781009157896.007, 2023.

520   Curcoll, R., Morguí, J. A., Kamnang, A., Cañas, L., Vargas, A., and Grossi, C.: Metrology for low-cost CO_2 sensors applications: the case of a steady-state through-flow (SS-TF) chamber for CO_2 fluxes observations, Atmos. Meas. Tech., 15, 2807–2818, 10.5194/amt-15-2807-2022, 2022.

Delaria, E. R., Kim, J., Fitzmaurice, H. L., Newman, C., Wooldridge, P. J., Worthington, K., and Cohen, R. C.: The Berkeley Environmental Air-quality and CO_2 Network: field calibrations of sensor
525   temperature dependence and assessment of network scale CO_2 accuracy, Atmospheric Measurement Techniques, 14, 5487–5500, 10.5194/amt-14-5487-2021, 2021.

Dubey, R., Telles, A., Nikkel, J., Cao, C., Gewirtzman, J., Raymond, P. A., and Lee, X.: Low-Cost CO(2) NDIR Sensors: Performance Evaluation and Calibration Using Machine Learning Techniques, Sensors (Basel), 24, 10.3390/s24175675, 2024.

530   Fang, S. X., Zhou, L. X., Tans, P. P., Ciais, P., Steinbacher, M., Xu, L., and Luan, T.: In situ measurement of atmospheric CO_2 at the four WMO/GAW stations in China, Atmospheric Chemistry and Physics, 14, 2541–2554, 10.5194/acp-14-2541-2014, 2014.

Friedlingstein, P., O'Sullivan, M., Jones, M. W., Andrew, R. M., Hauck, J., Olsen, A., Peters, G. P., Peters, W., Pongratz, J., Sitch, S., Le Quéré, C., Canadell, J. G., Ciais, P., Jackson, R. B., Alin, S., Aragão,
535   L. E. O. C., Arneth, A., Arora, V., Bates, N. R., Becker, M., Benoit-Cattin, A., Bittig, H. C., Bopp, L., Bultan, S., Chandra, N., Chevallier, F., Chini, L. P., Evans, W., Florentie, L., Forster, P. M., Gasser, T., Gehlen, M., Gilfillan, D., Gkritzalis, T., Gregor, L., Gruber, N., Harris, I., Hartung, K., Haverd, V., Houghton, R. A., Ilyina, T., Jain, A. K., Joetzjer, E., Kadono, K., Kato, E., Kitidis, V., Korsbakken, J. I., Landschützer, P., Lefèvre, N., Lenton, A., Lienert, S., Liu, Z., Lombardozzi, D., Marland, G., Metzl, N.,
540   Munro, D. R., Nabel, J. E. M. S., Nakaoka, S.-I., Niwa, Y., O'Brien, K., Ono, T., Palmer, P. I., Pierrot, D., Poulter, B., Resplandy, L., Robertson, E., Rödenbeck, C., Schwinger, J., Séférian, R., Skjelvan, I., Smith, A. J. P., Sutton, A. J., Tanhua, T., Tans, P. P., Tian, H., Tilbrook, B., van der Werf, G., Vuichard, N., Walker, A. P., Wanninkhof, R., Watson, A. J., Willis, D., Wiltshire, A. J., Yuan, W., Yue, X., and Zaehle, S.: Global Carbon Budget 2020, Earth System Science Data, 12, 3269–3340, 10.5194/essd-12-
545   3269-2020, 2020.

Friedlingstein, P., O'Sullivan, M., Jones, M. W., Andrew, R. M., Bakker, D. C. E., Hauck, J., Landschützer, P., Le Quéré, C., Luijkx, I. T., Peters, G. P., Peters, W., Pongratz, J., Schwingshackl, C., Sitch, S., Canadell, J. G., Ciais, P., Jackson, R. B., Alin, S. R., Anthoni, P., Barbero, L., Bates, N. R., Becker, M., Bellouin, N., Decharme, B., Bopp, L., Brasika, I. B. M., Cadule, P., Chamberlain, M. A.,
550   Chandra, N., Chau, T.-T.-T., Chevallier, F., Chini, L. P., Cronin, M., Dou, X., Enyo, K., Evans, W., Falk, S., Feely, R. A., Feng, L., Ford, D. J., Gasser, T., Ghattas, J., Gkritzalis, T., Grassi, G., Gregor, L., Gruber, N., Gürses, Ö., Harris, I., Hefner, M., Heinke, J., Houghton, R. A., Hurtt, G. C., Iida, Y., Ilyina, T., Jacobson, A. R., Jain, A., Jarníková, T., Jersild, A., Jiang, F., Jin, Z., Joos, F., Kato, E., Keeling, R. F., Kennedy, D., Klein Goldewijk, K., Knauer, J., Korsbakken, J. I., Körtzinger, A., Lan, X., Lefèvre, N.,
555   Li, H., Liu, J., Liu, Z., Ma, L., Marland, G., Mayot, N., McGuire, P. C., McKinley, G. A., Meyer, G., Morgan, E. J., Munro, D. R., Nakaoka, S.-I., Niwa, Y., O'Brien, K. M., Olsen, A., Omar, A. M., Ono, T.,

Paulsen, M., Pierrot, D., Pocock, K., Poulter, B., Powis, C. M., Rehder, G., Resplandy, L., Robertson, E., Rödenbeck, C., Rosan, T. M., Schwinger, J., Séférian, R., Smallman, T. L., Smith, S. M., Sospedra-Alfonso, R., Sun, Q., Sutton, A. J., Sweeney, C., Takao, S., Tans, P. P., Tian, H., Tilbrook, B., Tsujino, H., Tubiello, F., van der Werf, G. R., van Ooijen, E., Wanninkhof, R., Watanabe, M., Wimart-Rousseau, C., Yang, D., Yang, X., Yuan, W., Yue, X., Zaehle, S., Zeng, J., and Zheng, B.: Global Carbon Budget 2023, Earth System Science Data, 15, 5301–5369, 10.5194/essd-15-5301-2023, 2023.

Han, P., Yao, B., Cai, Q., Chen, H., Sun, W., Liang, M., Zhang, X., Zhao, M., Martin, C., Liu, Z., Ye, H., Wang, P., Li, Y., and Zeng, N.: Support Carbon Neutral Goal with a High-Resolution Carbon Monitoring System in Beijing, Bulletin of the American Meteorological Society, 105, E2461–E2481, 10.1175/bams-d-23-0025.1, 2024.

Jacobson, A. R., Mikaloff Fletcher, S. E., Gruber, N., Sarmiento, J. L., and Gloor, M.: A joint atmosphere-ocean inversion for surface fluxes of carbon dioxide: 2. Regional results, Global Biogeochemical Cycles, 21, 10.1029/2006gb002703, 2007.

Karion, A., Callahan, W., Stock, M., Prinzivalli, S., Verhulst, K. R., Kim, J., Salameh, P. K., Lopez-Coto, I., and Whetstone, J.: Greenhouse gas observations from the Northeast Corridor tower network, Earth System Science Data, 12, 699–717, 10.5194/essd-12-699-2020, 2020.

Landschützer, P., Gruber, N., Bakker, D. C. E., Schuster, U., Nakaoka, S., Payne, M. R., Sasse, T. P., and Zeng, J.: A neural network-based estimate of the seasonal to inter-annual variability of the Atlantic Ocean carbon sink, Biogeosciences, 10, 7793–7815, 10.5194/bg-10-7793-2013, 2013.

Li, D., Ni, X., Wang, K., Zeng, D., Wang, B., Jin, H., Li, H., Zhou, F., Huang, D., and Chen, J.: Biological CO_2 Uptake and Upwelling Regulate the Air-Sea CO_2 Flux in the Changjiang Plume Under South Winds in Summer, Frontiers in Marine Science, 8, 10.3389/fmars.2021.709783, 2021.

Li, Q., Guo, X., Zhai, W., Xu, Y., and Dai, M.: Partial pressure of CO_2 and air-sea CO_2 fluxes in the South China Sea: Synthesis of an 18-year dataset, Progress in Oceanography, 182, 10.1016/j.pocean.2020.102272, 2020.

Lin, X., Ciais, P., Bousquet, P., Ramonet, M., Yin, Y., Balkanski, Y., Cozic, A., Delmotte, M., Evangeliou, N., Indira, N. K., Locatelli, R., Peng, S., Piao, S., Saunois, M., Swathi, P. S., Wang, R., Yver-Kwok, C., Tiwari, Y. K., and Zhou, L.: Simulating CH4 and CO_2 over South and East Asia using the zoomed chemistry transport model LMDz-INCA, Atmospheric Chemistry and Physics, 18, 9475–9497, 10.5194/acp-18-9475-2018, 2018.

Lv, H., Wang, H., Jiang, Y., Chen, H., Qiao, R., and Wang, Z.: Study on the concentration variation of CO_2 in the background area of Xisha., Haiyang Xuebao, 37, 21–30, 10.3969/j.issn.0253-4193.2015.06.003, 2015.

Martin, C. R., Zeng, N., Karion, A., Dickerson, R. R., Ren, X., Turpie, B. N., and Weber, K. J.: Evaluation and environmental correction of ambient CO_2 measurements from a low-cost NDIR sensor, Atmospheric Measurement Techniques, 10, 2383–2395, 10.5194/amt-10-2383-2017, 2017.

Nemoto, K., Midorikawa, T., Wada, A., Ogawa, K., Takatani, S., Kimoto, H., Ishii, M., and Inoue, H. Y.: Continuous observations of atmospheric and oceanic CO_2 using a moored buoy in the East China Sea: Variations during the passage of typhoons, Deep Sea Research Part II: Topical Studies in Oceanography, 56, 542–553, 10.1016/j.dsr2.2008.12.015, 2009.

NOAA GML (2024a): About CO_2 measurements, National Oceanic and Atmospheric Administration, Global Monitoring Laboratory (GML), available at: https://gml.noaa.gov/ccgg/about/co2_measurements.html, last access: 12 November 2025.

600   NOAA GML (2024b): Trends in atmospheric carbon dioxide – Mauna Loa, National Oceanic and Atmospheric Administration, Global Monitoring Laboratory (GML), available at: https://gml.noaa.gov/ccgg/trends/gr.html, last access: 12 November 2025.

Palter, J. B., Nickford, S., and Mu, L.: Ocean Carbon Dioxide Uptake in the Tailpipe of Industrialized Continents, Geophysical Research Letters, 50, 10.1029/2023gl104822, 2023.

605   Piao, S., He, Y., Wang, X., and Chen, F.: Estimation of China's terrestrial ecosystem carbon sink: Methods, progress and prospects, Science China Earth Sciences, 65, 641–651, 10.1007/s11430-021-9892-6, 2022.

Rhein, M., Rintoul, S. R., Aoki, S., Campos, E., Chambers, D., Feely, R. A., Gulev, S., Johnson, G. C., Josey, S. A., Kostianoy, A., Mauritzen, C., Roemmich, D., Talley, L. D., and Wang, F.: Observations:

610   Ocean, in: Climate Change 2013: The Physical Science Basis. Contribution of Working Group I to the Fifth Assessment Report of the Intergovernmental Panel on Climate Change, edited by: Stocker, T. F., Qin, D., Plattner, G.-K., Tignor, M., Allen, S. K., Boschung, J., Nauels, A., Xia, Y., Bex, V., and Midgley, P. M., Cambridge University Press, Cambridge, United Kingdom and New York, NY, USA, 255–316, 10.1017/CBO9781107415324.010, 2013.

615   Rödenbeck, C., Conway, T. J., and Langenfelds, R. L.: The effect of systematic measurement errors on atmospheric CO_2 inversions: a quantitative assessment, Atmos. Chem. Phys., 6, 149–161, 10.5194/acp-6-149-2006, 2006.

Rolph, G., Stein, A., and Stunder, B.: Real-time Environmental Applications and Display sYstem: READY, Environmental Modelling & Software, 95, 210–228, 10.1016/j.envsoft.2017.06.025, 2017.

620   Sabine, C. L., Feely, R. A., Gruber, N., Key, R. M., Lee, K., Bullister, J. L., Wanninkhof, R., Wong, C. S., Wallace, D. W. R., Tilbrook, B., Millero, F. J., Peng, T.-H., Kozyr, A., Ono, T., and Rios, A. F.: The Oceanic Sink for Anthropogenic CO_2, Science, 305, 367–371, doi:10.1126/science.1097403, 2004.

Sarmiento, J. L., Johnson, K. S., Arteaga, L. A., Bushinsky, S. M., Cullen, H. M., Gray, A. R., Hotinski,

625   R. M., Maurer, T. L., Mazloff, M. R., Riser, S. C., Russell, J. L., Schofield, O. M., and Talley, L. D.: The Southern Ocean carbon and climate observations and modeling (SOCCOM) project: A review, Progress in Oceanography, 219, 10.1016/j.pocean.2023.103130, 2023.

Shusterman, A. A., Teige, V. E., Turner, A. J., Newman, C., Kim, J., and Cohen, R. C.: The BErkeley Atmospheric CO2 Observation Network: initial evaluation, Atmospheric Chemistry and Physics, 16,

630   13449–13463, 10.5194/acp-16-13449-2016, 2016.

Song, J., Qu, B., Li, X., Yuan, H., and Duan, L.: Estimate of Ocean Carbon Sink: Current Status and Reflections, Advances in Marine Science, 41, 577–592, 10.12362/j.issn.1671-6647.20230210001, 2023.

Thoning, K. W., Crotwell, A. M., and Mund, J. W.: Atmospheric Carbon Dioxide Dry Air Mole Fractions from continuous measurements at Mauna Loa, Hawaii, Barrow, Alaska, American Samoa, and South

635   Pole, 1973–present [dataset], 10.5194/amt-10-2383-2017, 2025.

Wanninkhof, R., Park, G.-H., Takahashi, T., Feely, R. A., Bullister, J. L., and Doney, S. C.: Changes in deep-water CO2 concentrations over the last several decades determined from discrete pCO2measurements, Deep Sea Research Part I: Oceanographic Research Papers, 74, 48–63, 10.1016/j.dsr.2012.12.005, 2013.

640   Wanninkhof, R., Pickers, P. A., Omar, A. M., Sutton, A., Murata, A., Olsen, A., Stephens, B. B., Tilbrook, B., Munro, D., Pierrot, D., Rehder, G., Santana-Casiano, J. M., Müller, J. D., Trinanes, J., Tedesco, K., O'Brien, K., Currie, K., Barbero, L., Telszewski, M., Hoppema, M., Ishii, M., González-Dávila, M.,

Bates, N. R., Metzl, N., Suntharalingam, P., Feely, R. A., Nakaoka, S.-i., Lauvset, S. K., Takahashi, T., Steinhoff, T., and Schuster, U.: A Surface Ocean CO2 Reference Network, SOCONET and Associated

645   Marine Boundary Layer CO2 Measurements, Frontiers in Marine Science, 6, 10.3389/fmars.2019.00400, 2019.

Xu, J., Cai, S., Xuan, L., Qiu, Y., and Zhu, D.: Study on coastal upwelling in eastern Hainan Island and western Guangdong in summer,2006, Acta Oceanologica Sinica(in Chinese), 35, 11–18, 2013.

Xu, S., Park, K., Wang, Y., Chen, L., Qi, D., and Li, B.: Variations in the summer oceanic pCO2 and

650   carbon sink in Prydz Bay using the self-organizing map analysis approach, Biogeosciences, 16, 797–810, 10.5194/bg-16-797-2019, 2019.

Yasuda, T., Yonemura, S., and Tani, A.: Comparison of the characteristics of small commercial NDIR CO2 sensor models and development of a portable CO2 measurement device, Sensors (Basel), 12, 3641–3655, 10.3390/s120303641, 2012.

655   Yu, S., Song, Z., Bai, Y., Guo, X., He, X., Zhai, W., Zhao, H., and Dai, M.: Satellite-estimated air-sea CO2 fluxes in the Bohai Sea, Yellow Sea, and East China Sea: Patterns and variations during 2003–2019, Science of The Total Environment, 904, 10.1016/j.scitotenv.2023.166804, 2023.

Zhai, W. D., Dai, M. H., Chen, B. S., Guo, X. H., Li, Q., Shang, S. L., Zhang, C. Y., Cai, W. J., and Wang, D. X.: Seasonal variations of sea–air CO2 fluxes in the largest tropical marginal sea (South China

660   Sea) based on multiple-year underway measurements, Biogeosciences, 10, 7775–7791, 10.5194/bg-10-7775-2013, 2013.

Zhang, G., Han, B., Yang, Q., Zhu, X., Wang, X., He, H., Li, H., Wang, X., Xie, W., and Chen, D.: Seamounts Enhance the Local Emission of CO2 in the Northern South China Sea, Geophysical Research Letters, 51, 10.1029/2023gl107264, 2024.